HELIUM LINE FORMATION AND ABUNDANCE IN A SOLAR ACTIVE REGION

P. J. D. Mauas

Instituto de Astronomía y Física del Espacio, Buenos Aires, Argentina; pablo@iafe.uba.ar

V. Andretta

INAF–Osservatorio Astronomico di Capodimonte, Salita Moiariello 16, 80131 Napoli, Italy

A. Falchi

INAF–Osservatorio Astrofisico di Arcetri, Largo Enrico Fermi 5, 50125 Firenze, Italy

R. Falciani

Dipartimento di Astronomia e Scienza dello Spazio, Università di Firenze, Largo Fermi 5, 50125 Firenze, Italy

L. Teriaca

Max-Planck-Institut für Sonnensystemforschung, Max-Planck-Strasse 2, 37191 Katlenburg-Lindau, Germany

AND

G. Cauzzi

INAF–Osservatorio Astrofisico di Arcetri, Largo Enrico Fermi 5, 50125 Firenze, Italy

Received 2004 September 9; accepted 2004 October 3

ABSTRACT

An observing campaign (*SOHO* JOP 139), coordinated between ground-based and *Solar and Heliospheric Observatory* (*SOHO*) instruments, has been planned to obtain simultaneous spectroheliograms of the same active region in several spectral lines. The chromospheric lines Ca II K, Hα, and Na I D, as well as He I 10830, 5876, 584, and He II 304 Å lines have been observed. The EUV radiation in the range $\lambda < 500$ Å and in the range $260 < \lambda < 340$ Å has also been measured at the same time. These simultaneous observations allow us to build semiempirical models of the chromosphere and low transition region of an active region, taking into account the estimated total number of photoionizing photons impinging on the target active region and their spectral distribution. We obtained a model that matches very well all the observed line profiles, using a standard value for the He abundance ([He] = 0.1) and a modified distribution of microturbulence. For this model we study the influence of the coronal radiation on the computed helium lines. We find that, even in an active region, the incident coronal radiation has a limited effect on the UV He lines, while it is of fundamental importance for the D3 and 10830 Å lines. Finally, we build two more models, assuming values of He abundance [He] = 0.07 and 1.5, only in the region where temperatures are $>1 \times 10^4$ K. This region, between the chromosphere and transition region, has been indicated as a good candidate for processes that might be responsible for strong variations of [He]. The set of our observables can still be well reproduced in both cases, changing the atmospheric structure mainly in the low transition region. This implies that, to choose between different values of [He], it is necessary to constrain the transition region with different observables, independent of the He lines.

Subject headings: Sun: abundances — Sun: activity

1. INTRODUCTION

Helium is a very peculiar element in the sense that, despite its high abundance in the universe, its photospheric solar abundance is unknown. Unfortunately, it is undetectable in the visible photospheric spectrum and, until recently, the so-called solar photospheric abundance has been derived using theoretical stellar evolution models. A commonly accepted value for the ratio [He] = $N_{\mathrm{He}}/N_{\mathrm{H}}$ is 0.1 and represents the helium abundance of the nebula from which the solar system formed. However, there are now strong indications that this value is too large: the inversion of helioseismic data by different authors leads to values of [He], in the convection zone, in the range 0.078–0.088 (for a review, see Boothroyd & Sackmann 2003). A reduction of He abundance of roughly 10% below its initial value could be explained including diffusion in the theoretical evolution models (Proffitt & Michaud 1991; Boothroyd & Sackmann 2003).

The values quoted above refer to the outer convection zone and to the photosphere. Measurements of [He] in the solar wind and interplanetary medium exhibit a high variability, from almost negligible values (∼0.01) in equatorial regions to high values (∼0.3) in transient events. An average value in the fast component of the solar wind is about 0.05, thus about a factor of 2 lower than the photospheric [He] (Barraclough et al. 1995; Bochsler 1998). This value is also in contrast to the general pattern of abundance variations in the fast wind, in which elements with first ionization potential (FIP) ≥10 eV typically retain their photospheric abundance as opposed to low-FIP elements (≤10 eV), which appear enhanced (for a review, see Meyer 1996).

Direct measurements of [He] in the solar atmosphere closer to the surface are available only for the corona. In the quiet corona, at $R \approx 1.1\ R_\odot$, Gabriel et al. (1995) and Feldman (1998) found [He] ≈ 0.08, suggesting no helium depletion in the low corona, while in an equatorial streamer, at $R \approx 1.5\ R_\odot$, Raymond et al. (1997) found an upper limit of 0.05. More recently, Laming & Feldman (2001, 2003) have estimated an abundance of 0.05 and 0.04, respectively, at distances $R < 1.1\ R_\odot$.

Apart from the observed variability and/or inconsistencies of the measurements in the corona and the solar wind, the general

pattern of the FIP effect suggests that elemental fractionation should occur in the chromosphere at $T < 10^4$ K (Geiss 1982). Detailed theoretical calculations including diffusion effects (Hansteen et al. 1997; Lie-Svendsen et al. 2003) seem to confirm that, indeed, [He] undergoes strong changes from the chromosphere to the lower corona before stabilizing at the values observed in the solar wind.

Therefore, it would be very important to determine the He abundance at chromospheric and transition region levels directly from line profiles. The strongest He lines in the solar atmosphere are in the extreme ultraviolet (EUV) below 584 Å. From the ground, the only observable He line in the quiet solar atmosphere (on the disk) is in the near-infrared at 10830 Å, but when active regions or flares are observed the He lines are enhanced, and in particular, the D3 line at 5876 Å can also be detected. The excitation of these subordinate lines is at least partially due to a photoionization-recombination mechanism or "PR" process (Zirin 1975; Andretta & Jones 1997), i.e., to direct photoionization of chromospheric helium atoms by coronal EUV radiation shortward of 504 Å and successive recombination to the excited levels of He I. Observations actually suggest that this process might not be very important in quiescent regions, at least for the strong resonance, hydrogen-like He II lines such as the Lyα at 304 Å (e.g., Fontenla et al. 1993; Andretta et al. 2000, 2003). However, no conclusive determination of the role of this process is available yet for active regions (e.g., Fredvick & Maltby, 1999), where the coronal EUV radiation field is much more intense than in quiet areas. Hence, the study of the solar He spectrum requires not only spectral observations of an active region (or flare) in a very large spectral range (from EUV to near-infrared) but also an estimate of the coronal EUV radiation impinging on the observed active region.

To this aim we planned an observing campaign (*SOHO* JOP 139) coordinated between ground-based and *Solar and Heliospheric Observatory* (*SOHO*) instruments to obtain simultaneous spectroheliograms of the same area in several spectral lines, including four He lines, that sample the solar atmosphere from the chromosphere to the transition region. During this campaign we observed the region NOAA AR 9468 (cos θ = 0.99) on 2001 May 26 from 13:00 to 18:00 UT. A small two-ribbon flare (*GOES* class C1), developed in this region around 16 UT, and its dynamics during the impulsive phase has been already studied in Teriaca et al. (2003).

In this paper we concentrate on the preflare phase. We present semiempirical models of the atmosphere of the active region (at 15:20 UT) constructed to match the observed line profiles from the chromosphere to the transition region and taking into account the EUV radiation in the range $1-500$ Å. The comparison between the observed and computed He line profiles allowed us to test the relevance of the PR process and of the He abundance values in an active region. In a later paper we will study the formation of He lines in the flare.

2. OBSERVATIONS

A detailed description of the observing program is given in Teriaca et al. (2003). We recall here that spectroheliograms were acquired with the Horizontal Spectrograph at the Dunn Solar Telescope (DST) of the National Solar Observatory at Sacramento Peak in the chromospheric lines Ca II K, Hα, and Na I D, as well as in the He I lines at 5876 (D3) and 10830 Å. The full field of view (FOV) of the DST, $170'' \times 170''$, was covered in about 5 minutes with a sampling step of $2''$. Correcting for offsets among the different detectors resulted in a final useful FOV of $160'' \times 140''$ with an effective resolution of $2''$.

During the same period, spectroheliograms of the active region were obtained in the spectral windows around the He I 584 Å and the He II 304 Å spectral lines with the Normal Incidence Spectrometer (NIS) of the Coronal Diagnostic Spectrometer (CDS) aboard *SOHO*. The slit was stepped $6''$, covering a $148''$ wide area in ∼5.5 minutes. The final useful FOV was $148'' \times 138''$ with an effective resolution of $6'' \times 3''.4$. Ground-based and CDS data were aligned using *SOHO* MDI images as a reference. We estimate the error to be around a few arcseconds. CDS and ground-based spectra are simultaneous within 2 minutes.

The EUV flux was monitored by the Solar EUV Monitor (SEM) instrument aboard *SOHO* (Hovestadt et al. 1995). The CELIAS/SEM instrument provides calibrated total photon counts in the range $\lambda < 500$ Å (zeroth order, SEM_0) and in the range $260 < \lambda < 340$ Å (first order, SEM_1) at 1 AU.

Finally, the EUV Imaging Telescope (EIT; Delaboudinière et al. 1995) provided a synoptic series of full-disk images centered on 171, 195, 284, and 304 Å around 13:00 and 19:00 UT.

3. DERIVATION OF THE PHOTOIONIZING RADIATION

In § 1 we mentioned the role of EUV radiation, emitted mainly by coronal plasma, in the excitation of helium lines. The relevant radiation we need to estimate falls in the wavelength range below the photoionization threshold of He I at 504 Å (the photoionization threshold for He II is at 228 Å). A misconception, commonly found in the literature, is that it would be sufficient to have an estimate of the intensities just near the photoionization thresholds because of the sharp decrease with wavelength of the photoionization cross sections, which are proportional to $\sim\lambda^2$ and $\sim\lambda^3$ for He I and He II, respectively. However, as discussed in more detail by Andretta et al. (2003), even photons of considerably shorter wavelength can efficiently photoionize helium atoms and ions; what matters most is the *ratio* between helium and hydrogen photoionization cross sections, at least for $\lambda > 20-50$ Å (at shorter wavelengths, inner-shell photoionization of metals absorb most of the photons). The wavelength of the photoionizing photons mainly determines how deeply in the atmosphere they can penetrate, since the photoionization absorption cross sections decrease with wavelength. This point will be further illustrated in § 4.3.

Therefore, for the calculation of the He line profiles we needed to estimate the total number of photoionizing photons impinging on the target active region plus their spectral distribution. We obtained reliable estimates of these quantities combining both observational constraints from CELIAS/SEM and EIT and theoretical tools. The adopted procedures are illustrated in the following sections.

3.1. *Coronal Irradiance*

The solar irradiances measured at about 15:20 UT in the SEM_0 and SEM_1 wavebands are $\Phi^{\mathrm{SEM}_0} = 5.05 \times 10^{10}$ photons cm^{-2} s^{-1} and $\Phi^{\mathrm{SEM}_1} = 2.57 \times 10^{10}$ photons cm^{-2} s^{-1}, respectively, with noiselike variations of the order of 0.1%. Even the subsequent C1.1 class flare, starting at 16:01 UT (Teriaca et al. 2003), produced variations in the SEM irradiances limited to at most 1%.

Both quantities include the contribution of the He II 304 Å line, while Φ^{SEM_0} also contains the other He II resonance features. Since the He lines and continua will be self-consistently computed in our radiative transfer calculations, we need to exclude those contributions to obtain the input values for our model calculations.

The He II 256 Å line has been observed to be at least 15 times weaker than the 304 Å line in quiet regions (Mango et al. 1978).

For an active region, observations of the first four terms of the resonance series indicate that the He II 304 Å is at least 40 times more intense than the 256 Å line and about 25 times more intense than the sum of the 256, 243, and 237 Å terms (Thomas & Neupert 1994). Evaluating the contribution of the continuum at $\lambda < 228$ Å is considerably more difficult (see, for instance, Andretta et al. 2003). In an optically thin recombination spectrum, the contribution of that continuum could be as high as 30% of the total number of photons. However, the existing observations of the resonance series (such as those cited above) strongly suggest a formation of the He II spectrum at high optical depths. Therefore, we may expect a considerably smaller contribution of the continuum and of other lines, as already suggested by Zirin (1975) and Athay (1988). Overall, we thus estimate that the contribution of the He II features below 256 Å is less than 10% of that of the He II 304 Å line, so that only the latter line need be taken into account in the measured SEM irradiances.

The contribution of the He II 304 Å line (plus the nearby Si XI 303 Å line) to SEM_1 irradiances has been estimated by Thompson et al. (2002) at approximately 50%–60% for observations acquired during 2001. Adopting an average value of 55%, $\Phi^{He+Si} = 1.4 \times 10^{10}$ photons cm^{-2} s^{-1} (the contribution of the Si XI 303 Å line is about 10%).

Subtracting this value from the SEM_0 irradiances, we obtain the solar irradiance due to coronal lines only: $\Phi^{corona} \approx 3.64 \times 10^{10}$ photons cm^{-2} s^{-1}. The uncertainty in this value is mainly due to the uncertainty in the absolute calibration of the He II 304 Å line relative to the other lines in the CDS spectra used by Thompson et al. (2002). For CDS, the maximum uncertainty of the second-order calibration, relevant for the He II 304 Å line, can be conservatively estimated at $\sim$30% (Andretta et al. 2003). Thus, the above value of Φ^{He+Si} has a maximum relative error of $\sim$14%, which translates into a maximum error of 0.2×10^{10} photons cm^{-2} s^{-1} for Φ^{corona}. If we assimilate this maximum error to a 3 σ uncertainty, the standard deviation for Φ^{corona} can be estimated to be $\sim 0.06 \times 10^{10}$ photons cm^{-2} s^{-1}. We thus finally obtain: $\Phi^{corona} = (3.6 \pm 0.1) \times 10^{10}$ photons cm^{-2} s^{-1} (1 σ error). In the estimated uncertainty for this value, we can safely include the errors introduced by neglecting the contributions of the Si XI 303 Å lines and of the other He II features, contributions that should be roughly of the same order, as mentioned above, but of opposite sign.

3.2. Total Number of Ionizing Photons at the Solar Surface

To obtain the contribution from the area around the DST slit to the total EUV solar irradiance we used the spatial distribution of EUV emission provided by EIT images. The details of the method are described in the Appendix and we illustrate here only the main assumptions and results. Basically, to obtain the mean value of I^{SEM_0} and I^{SEM_1} in any region of the EIT FOV, we scale the SEM-calibrated irradiances, Φ^{SEM_0} and Φ^{SEM_1}, by the ratio of the mean counts in the region over the total counts in the full EIT FOV (eq. [A4]).

This procedure assumes that the total counts over the detector in an EIT band (after basic CCD processing, including flat-fielding) are proportional to the irradiance, Φ^{EIT}, in the same band. This is true if the contribution to Φ^{EIT} from the corona beyond $1.2–1.4$ $R_\odot$ (the limit of an EIT image) is negligible. In fact, inspection of the EIT images used in our analysis reveals that only a small fraction of counts comes from areas above 1.1 $R_\odot$, and most of those counts are probably due to light scattered in the telescope.

The strongest assumption in this procedure, however, is that the images in the EIT wavebands are good linear proxies of the intensity integrated within the SEM wavebands. In the case of the $\lambda < 500$ Å range (SEM_0), all EIT bands (around 171, 195, 284, and 304 Å) include strong lines that contribute significantly to the total flux in that range. Thus, we may expect such an assumption to be quite reasonable. The case of the SEM_1 range is more straightforward: the EIT 304 waveband, although narrower, is centered at the same wavelength ($\sim$300 Å), and we may expect EIT 304 images to be good proxies of the spatial variation on the disk of the radiance in the SEM_1 waveband.

On the other hand, the assumption of linear correlation of EIT intensities with integrated intensities in the SEM wavebands is equivalent to assuming that the spectral distribution of EUV photons in those wavebands does not change with the location on the Sun and that only the overall intensity of the lines changes. This assumption is consistent with the calibration procedure of the SEM data (Judge et al. 1998) and is estimated to affect SEM_0 measurements by about 10% (McMullin et al. 2002).

Hence, we considered a region of $70'' \times 70''$ centered at the position of the DST slit (solar rotation being taken into account), and we computed the conversion factors from Φ^{SEM} to the mean value of I^{SEM} using two sets of EIT synoptic images taken before and after the DST and CDS observations (at 13:00 and 19:00 UT). Since we already subtracted the contribution of the He II 304 Å line to the SEM_0 irradiance, we did not consider the EIT 304 images. In this way, we obtained an average conversion factor $c = (3.3 \pm 0.6) \times 10^4$ sr^{-1}, for which the uncertainty was obtained from the standard deviation of the distribution of counts within the region of interest. Therefore, the intensity of coronal lines, integrated in the $\lambda < 500$ wavelength range and averaged over the area of the DST slit, is $I^{corona} = \Phi^{corona} c = (1.2 \pm 0.2) \times 10^{15}$ photons cm^{-2} s^{-1} sr^{-1}.

In order to validate this approach, we compare the intensity measured directly from CDS in the target area [$I^{He+Si} = (1.1 \pm 0.1) \times 10^{15}$ photons cm^{-2} s^{-1} sr^{-1}] with the one obtained from the SEM_1 irradiance using the described procedure. The mean conversion factor from the two synoptic EIT 304 images is $(5.8 \pm 2.5) \times 10^4$ sr^{-1} and therefore $I^{He+Si} = \Phi^{He+Si} c = (0.8 \pm 0.4) \times 10^{15}$ photons cm^{-2} s^{-1} sr^{-1}. The agreement between these estimates and the values measured with CDS is within the uncertainties.

3.3. Angular and Spectral Distribution of Photoionizing Photons

The values computed in the previous section refer to intensities incident perpendicularly to the solar surface. In our following calculations, we assume that the photoionizing incident intensities are constant with direction. It is very difficult to evaluate this assumption, since the variation with angle of the photoionizing radiation depends on the spatial distribution of the coronal plasma around the region of interest. For instance, had we assumed a vertically stratified, plane-parallel, optically thin corona, we would have obtained an intensity varying as $1/\mu$, where μ is the cosine of the angle with the normal. Under such an assumption, the variation of the mean intensity, J, (and thus of the photoionization rate) with optical depth, τ, is $J(\tau) \sim E_1(\tau)$, where $E_1(x)$ is the first exponential integral. The constant intensity case we adopted gives instead a dependence $J(\tau) \sim E_2(\tau)$. However, at large depths the two assumptions give the same result: $J(\tau) \sim \exp(-\tau)/\tau$. The differences are strong only in the shallower layers, with the ratio $E_2(\tau)/E_1(\tau)$ falling below 2 already for $\tau > 0.26$.
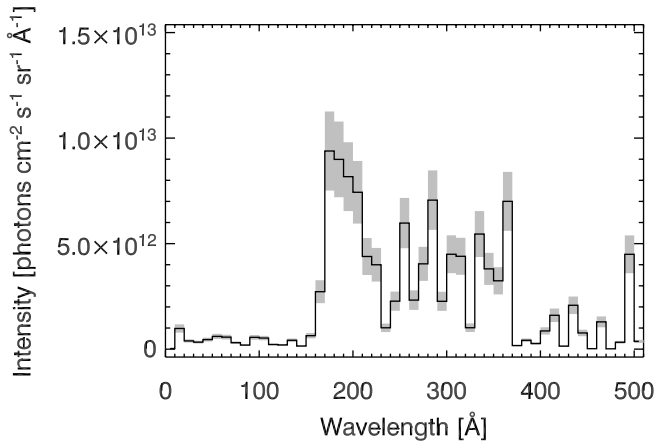
FIG. 1.—Estimated spectral distributions of photons around the DST slit, derived as described in § 3.3. The solid histogram shows the spectral distribution derived from a CHIANTI synthetic spectrum; the gray area indicates 1 σ uncertainties.

For the wavelength distribution of the ionizing photons, we adopt a synthetic spectrum obtained with the CHIANTI database (ver. 4; Young et al. 2003) with the differential emission measure (DEM) of an "average" active region from Vernazza & Reeves (1978). In the calculations, we used standard elemental abundances, with some values scaled to mimic the FIP effect (further details in the file sun_hybrid_ext.abund in the CHIANTI package), and a value $P_e/k = 3 \times 10^{15}$ K cm^{-3}, where P_e is the electron pressure and k the Boltzmann constant.

We need to scale the synthetic spectrum (excluding, of course, the He II lines and continua) by a factor 1.3 ± 0.3 to obtain the value of I^{corona} found in § 3.2. We note that such a linear scaling is equivalent to assuming that the shape of the DEM distribution of the plasma in our region of interest is the same as that of the distribution used to compute the synthetic spectrum. The resulting spectrum is shown in Figure 1.

4. ATMOSPHERIC MODELS

Our goal was the determination of semiempirical models of the chromosphere and low transition region of the active region, providing a good match with the observed line profiles. The diagnostics we used for the chromospheric part of the models were the profiles of the Ca II K, Hα, and Na I D lines, as well as the He I lines at 5876 Å (D3) and 10830 Å, averaged over a region of $6'' \times 3''.4$, which corresponds to the effective resolution of CDS. For the transition region we used the CDS profiles of the He I line at 584 Å and of the He II Lyα line at 304 Å.

4.1. General Characteristics

The modeling was done using the program PANDORA (Avrett & Loeser 1984, 2003). Given a T versus z distribution, we solved the non-LTE radiative transfer and the statistical and hydrostatic equilibrium equations and self-consistently computed non-LTE populations for 10 levels of H, 29 of He I, 15 of Fe I, 9 of C I, 8 of Si I, Ca I, and Na I, 6 of Al I and He II, and 7 of Mg I. In addition, we computed 6 levels of Mg II and 5 of Ca II.

More detail on the modeling and on the different assumptions and their validity can be found in Falchi & Mauas (1998). Here we just point out that the Ca II line profiles are computed in partial redistribution and that line blanketing is included, considering Kurucz's opacities. The atomic models we used for H and Ca II are described in Mauas et al. (1997) and Falchi & Mauas (1998). For He I, we used the 29 level model described in

Andretta & Jones (1997), which, apart for the number of levels, differs very slightly from the model of Fontenla et al. (1993). The different components in the lines were treated assuming that the sublevels are populated according to LTE, as explained in Mauas et al. (1988). For He II we used the six-level model of Fontenla et al. (1993).

The calculations include incident radiation from the coronal lines, which affects in particular the ionization balance in the H, He I, and He II continua. As explained in § 3.3, this radiation was obtained by scaling by a factor of 1.3 the distribution given by the CHIANTI database for an active region. As a starting point for the helium abundance, we used the standard photospheric value [He] = 0.1. The microturbulence followed the semiempirical distribution given by Fontenla et al. (1991) as a function of total hydrogen density.

As studied by Fontenla et al. (2002), the inclusion of ambipolar diffusion of helium can have an important effect in the construction of a model, changing the energy balance and therefore the T versus z structure. However, it must be remarked that their models of the low transition region are theoretical, while we adopt a semiempirical approach. We have made some trial runs including ambipolar diffusion, but keeping our atmospheric structure unchanged, and found that the emitted profiles remain unchanged.

4.2. Model Construction

Given the different sensitivity of various spectral lines to modifications in different parts of the model, we can describe its construction as a step by step process. The source function for Hα is sensitive to the structure of the chromosphere from the temperature minimum region to the base of the transition region, even if the line center is formed higher in the atmosphere. The Ca II K line, in particular its wings and the K1 minimum, are formed at the temperature minimum and in the low and mid-chromosphere. Therefore, we fixed the deeper part of the chromospheric structure using these two profiles and cross-checked it with the profile of the Na D lines, which are much less sensitive to these atmospheric layers. None of these lines depend on the coronal EUV radiation.

The profiles of the He I lines at 5876 Å (D3) and 10830 Å are formed in two distinct regions. Most of the radiation in both lines is originated in the photosphere, which in the quiet Sun results in a weak absorption line at 10830 Å and no noticeable line at 5876 Å. However, in an active region there is also a chromospheric contribution that depends mainly on the coronal EUV incident radiation but also on the thermal structure of the high-chromosphere low transition region between 1×10^4 and 2.5×10^4 K. We used these lines, therefore, to fix this region as a second step in the construction of the model.

Finally, both ultraviolet lines, the He I line at 584 Å and the He II line at 304 Å, depend on the structure of the low and mid-transition region from 3×10^4 to 5×10^4 K for the 584 Å line and up to 1×10^5 K for the 304 Å line. As mentioned in § 1, their dependence on the EUV coronal radiation is not yet assessed and should therefore be investigated. Hence, we used these lines in a final step as diagnostics of the structure of the transition region.

In Figure 2 we show the distribution of the temperature as a function of column mass for the model that gives the best match to the observations (dashed line). Also shown are the regions of formation of the different lines we used as diagnostics for the model construction.

In Figure 3 we show the computed and observed line profiles for the Hα, Ca II K, and Na D lines, which do not depend on the
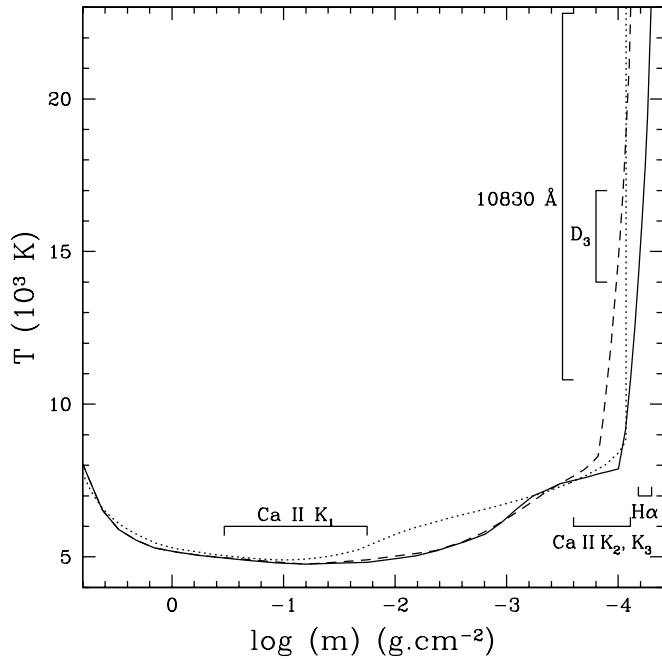
FIG. 2.—Temperature vs. column mass distribution of the computed atmospheric models. The models shown were obtained with the microturbulent velocity of Fontenla et al. (1991) (*dashed line*) and with a value of 5 km s^{-1} in the region of formation of the lines (*solid line*; see text). The plage model P (Fontenla et al. 1993) is displayed for reference (*dotted line*). Also shown are the heights of formation of the different lines we used to build the models. The He I 584 Å line is formed at temperatures between 2.4×10^4 and 3.4×10^4 K, and the He II 304 Å line is formed between 9.5×10^4 and 1×10^5 K.

FIG. 3.—Observed (*dashed line*) and computed (*solid line*) profiles for the Hα, Ca II K, and Na D lines. The bars indicate the rms of the averaged profiles (see text) and point out the variability between pixels.

radiation field. All computed profiles were convolved with the instrumental response. The bars in the figure indicate the rms of the profiles averaged over the area observed by CDS. It can be seen that the agreement found is very good, well within the rms.

In Figure 4 we compare the observed helium lines with the profiles obtained from this model, again convolved with the instrumental response. We want to stress that for the 584 Å line, the instrumental effects are rather heavy, washing out completely the strong central self-absorption of the computed profile (see § 4.3 and Fig. 6). The He II 304 Å line profile (not shown) is very similar to the 584 Å line. For all the helium lines, although the central intensities agree with the observations within the variability between pixels, the resulting computed profiles are too broad. Furthermore, the observed profile of the 10830 Å line distinctly shows the weak blue component of the triplet, which in the computed profile appears washed out.

The main parameter that contributes to the broadening of these lines is the microturbulent velocity (v_t). As described above, in this model we adopted the turbulence distribution given by Fontenla et al. (1991). To obtain a better match with the observed He lines, we then tried a different microturbulence distribution, changing v_t from 10 to 5 km s^{-1} in the region with temperature ranging from 1×10^4 to 2×10^4 K. Since the microturbulent velocity is included in the hydrostatic equilibrium equations, changing it implies changing the densities and therefore the atmospheric structure. Hence, the whole procedure was repeated until a satisfactory match with the observations was found, and a new model was built. This model is also shown in Figure 2 as a solid line, and the corresponding profiles for the He lines are shown in Figure 4. The new profiles for the Hα, Ca II K, and Na D lines (not shown) are very similar to the ones obtained with the former model. It can be seen that the match to He profiles is now strongly improved. We have therefore
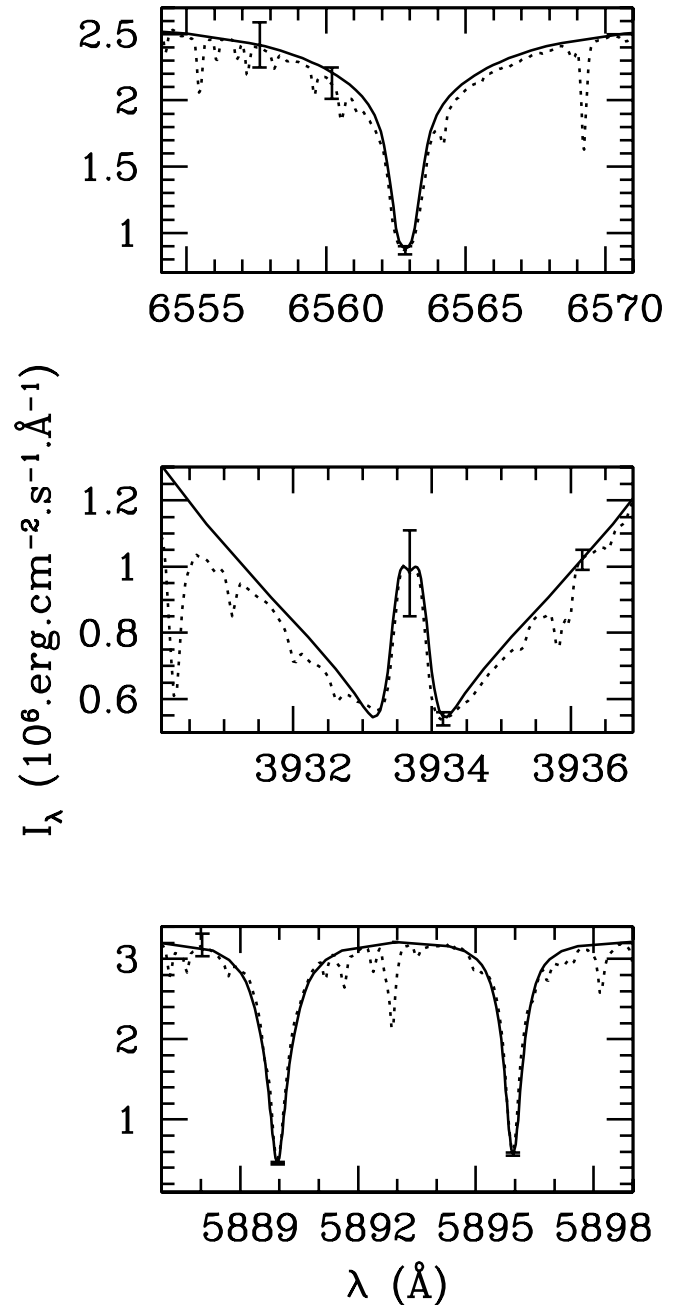
adopted this model as our standard model for the observed active region.

Finally, we checked a posteriori that the value of $P_e/k = 3 \times 10^{15}$ K cm^{-3}, assumed to compute the spectral distribution of the coronal radiation with the CHIANTI database, agrees with that found with our models. The most external point of the model for which we have an observational constraint has a temperature $T = 1.1 \times 10^5$ K and an electron density $N_e = 2.3 \times 10^{10}$ cm^{-3}, resulting in a very good agreement with $P_e/k = 2.5 \times 10^{15}$ K cm^{-3}.

4.3. *Effect of the EUV Radiation*

To assess the influence of the coronal radiation on the profiles of the helium lines, we performed new calculations for different
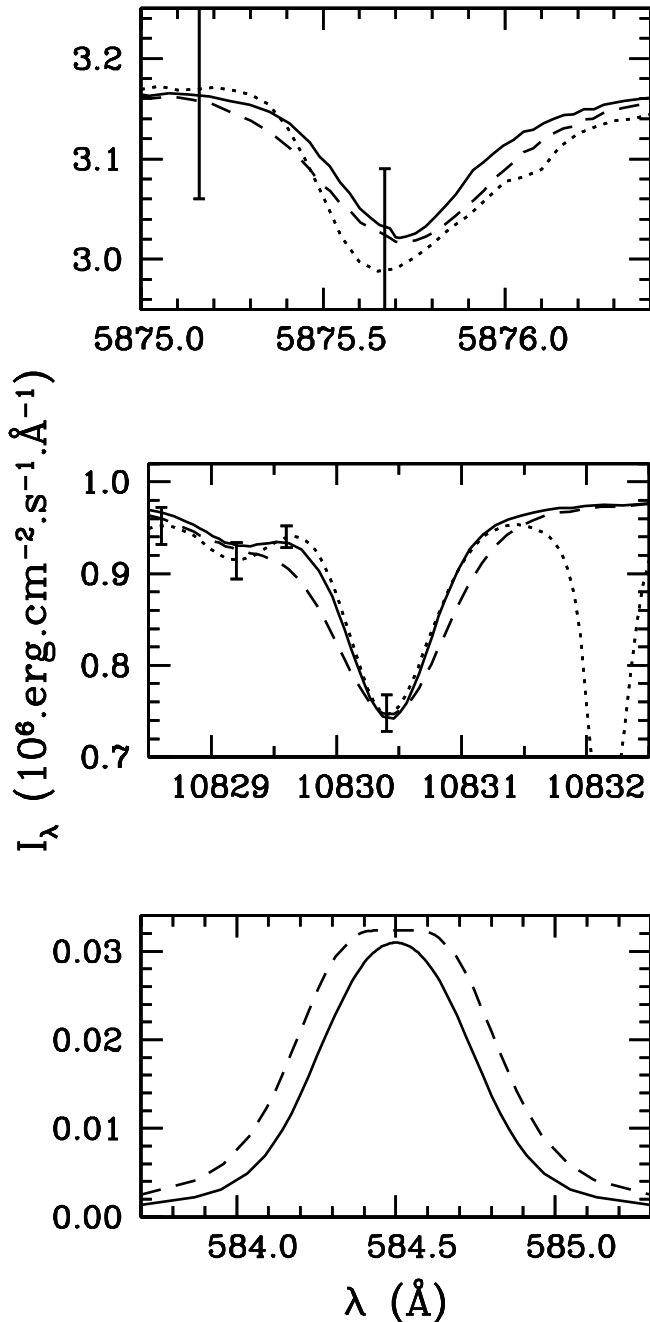
Fig. 4.—Comparison between observed and computed profiles of three helium lines. *Dotted line*: Observed. *Dashed line*: Computed profiles (convolved with instrumental response) for the model adopting the microturbulence of Fontenla et al. (1991). *Solid line*: Same as dashed but for our standard model where microturbulence has been reduced (see text). In the upper and middle panels, bars indicate the rms of the averaged profiles and point out the variability between pixels. For the shallow D3 line (maximum central depth ∼5%), the variability is very large and the bars are clipped at the limits of the plot.

Fig. 5.—Central intensity for the 10830 Å line as a function of the intensity I^{corona} for different step distributions of the field.

intensities of the radiation field and for different spectral distributions. Since the most important change in the profiles with the radiation field is in the central depth of the D3 and of the 10830 Å line, in Figure 5 we show the intensity in the center of the 10830 Å line as a function of the intensity I^{corona}.

Each curve in the figure represents a different spectral distribution. In each case, we considered a step function that is nonzero only in a limited spectral range and zero outside it. In this way, we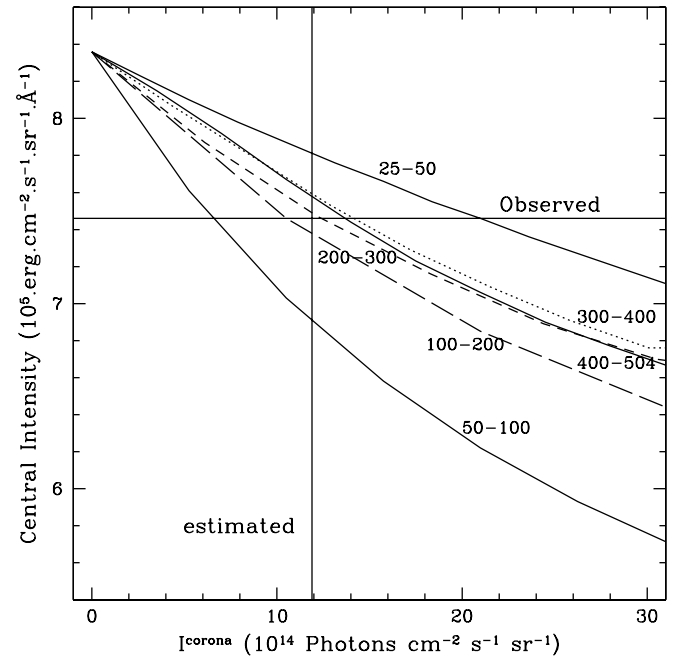 tested distributions with all the photons localized between 25 and 50, 50 and 100, 100 and 200, 200 and 300, 300 and 400, and 400 and 504 Å.

Several important conclusions can be drawn from this figure. First, photons at short wavelengths ($\lambda < 50$ Å) have a small influence on the line profiles. Second, for the same value of I^{corona}, photons between 50 and 100 Å are the most effective in increasing the line central intensity. Third, the details of the spectral distribution between 100 and 504 Å are of little relevance for the resulting central intensity.

Such effects, anticipated by Andretta et al. (2003) and reprised in § 3, can be understood in terms of the dependence on wavelength of the fraction of EUV photons effectively capable of photoionizing helium atoms and ions. The first effect is essentially due to the fact that short-wavelength photons are almost entirely absorbed by metals via inner-shell photoionizations. At longer wavelengths, the relevant parameter is the ratio of helium and hydrogen photoionization cross sections. The fact that the ratio between 50 and 100 Å is about 3–5 times the same ratio at 500 Å is consistent with the second conclusion drawn from Figure 5. Likewise, the third result can be understood by noting that the ratio between the He I and hydrogen cross sections changes in a relatively slow fashion at long wavelengths.

In light of these results, we note that, in principle, any given central intensity of the 10830 Å line could be obtained with different values of I^{corona} but only if assuming very different spectral distributions. For example, the observed central intensity can be obtained with 8×10^{14} photons cm^{-2} s^{-1} sr^{-1} between 50 and 100 Å or with almost twice as many photons between 300 and 504 Å. However, for a "stationary" active region such as in our case, the hypothesis of a dominant contribution at shorter wavelengths is rather implausible, so our assumption of a synthetic spectrum obtained with the CHIANTI database (§ 3.3) seems fully justified.

In Figure 6 we show the effect of the coronal radiation on the 584 Å profile. We compare the profiles for the 584 Å obtained with no incident coronal radiation with those obtained with $I^{corona} = 1 \times 10^{15}$ photons cm^{-2} s^{-1} sr^{-1} with two different spectral distributions. We see that the profiles are very similar and that
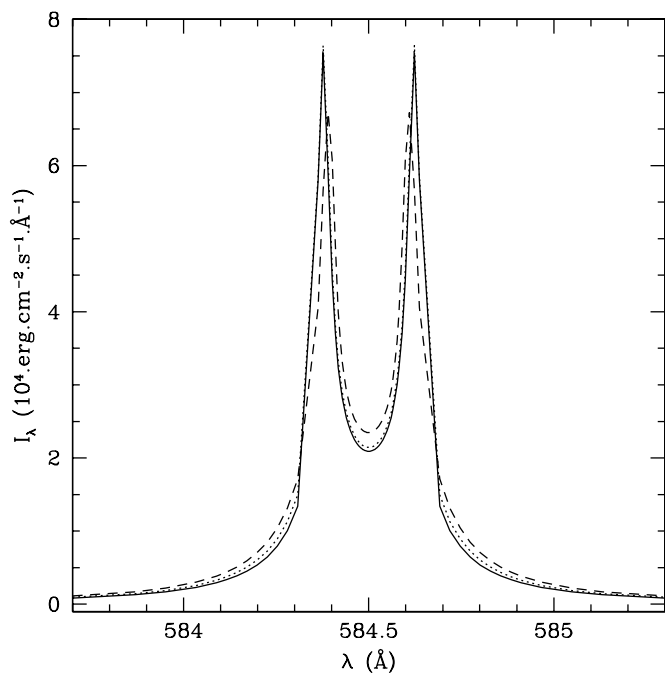
Fig. 6.—Profile for the 584 Å line computed with no incident coronal radiation (*solid line*), compared with the profiles computed for $I^{corona} = 1 \times 10^{15}$ photons cm^{-2} s^{-1} sr^{-1} but with different spectral distribution. The dashed line represents all photons between 400 and 504 Å, while the dotted line represents all photons between 50 and 100 Å.

the maximum difference (in the peak intensity) is about 10%. The profile variation depends more on the spectral distribution than on the intensity of coronal radiation. As expected, when all photons are between 50 and 100 Å and penetrate deeper in the atmosphere, the line does not change appreciably. A small change occurs instead when all photons are between 400 and 504 Å. We obtained a similar result for the He II 304 Å line.
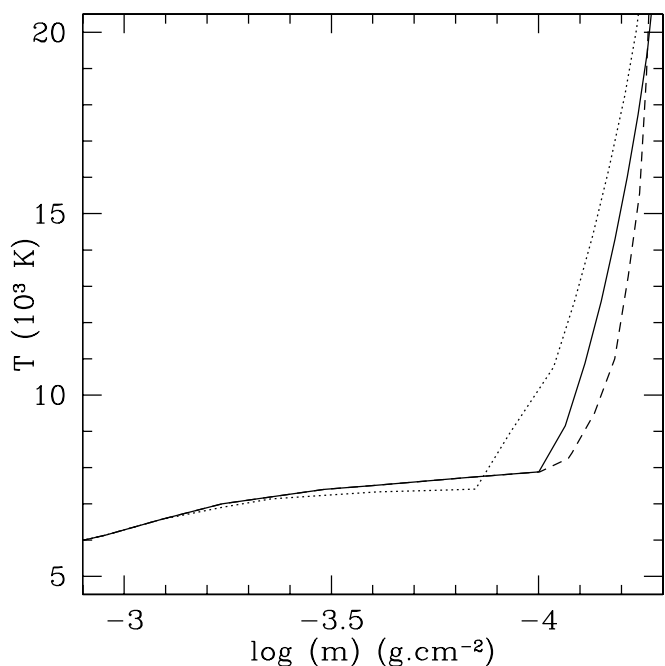

Fig. 7.—Temperature vs. column mass distribution of the atmospheric models obtained for different values of the He abundance in the region where they differ. The solid line represents [He] = 0.1, our standard model; the dotted line represents [He] = 0.07; the dashed line represents [He] = 0.15.
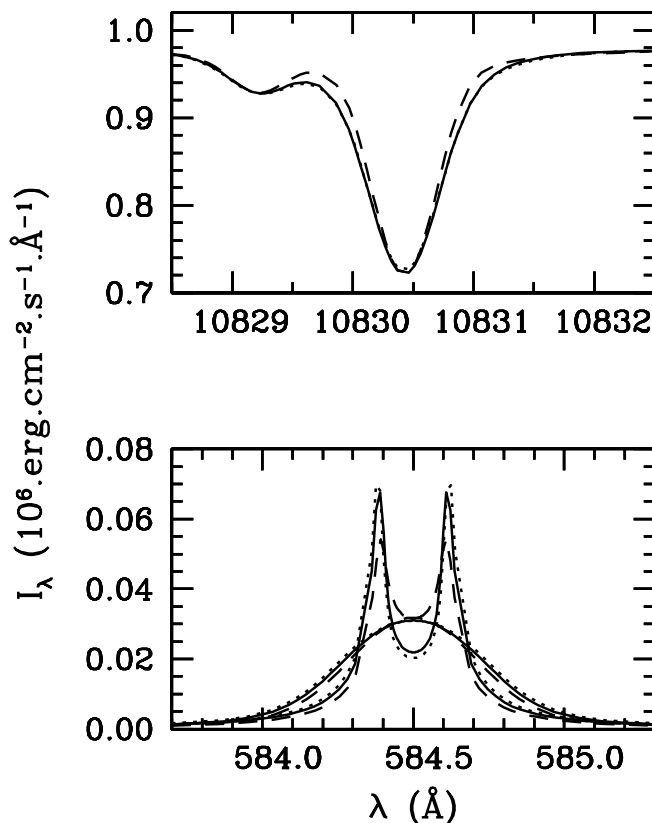

Fig. 8.—Profile for two helium lines for different values of the helium abundance. The solid line represents [He] = 0.1, our standard model; the dotted line represents [He] = 0.07; the dashed line represents [He] = 0.15. For the 584 Å line the profiles before the convolution with the instrumental response are also shown.

Our analysis hence shows that, similarly to the quiescent case, for active regions the coronal radiation has a much stronger effect on the chromospheric He lines than on the transition region He lines.

4.4. *Helium Abundance*

In the previous sections, we have shown how a semiempirical model employing the standard value of [He] = 0.1 can reproduce very well the observational data. On the other hand, the actual value of [He] in different parts of the solar atmosphere is a matter of discussion (see § 1), so it might be of interest to investigate how different values of [He] affect our computations.

Changing the abundance modifies the total density for a given height and therefore affects the hydrostatic equilibrium. Hence, modifying [He] in the whole solar atmosphere would result in a completely different atmospheric structure. In particular, the resulting photosphere could not be constrained by our observations. Furthermore, the region between the chromosphere and transition region has been indicated as a good candidate for processes that might be responsible for strong variations of [He] (Lie-Svendsen et al. 2003). For these reasons, we changed [He] only from the point where $T = 1. \times 10^4$ K outward, where the He lines are formed and recomputed the models until we found a satisfactory match with the observations. We built two different models, assuming values of the abundance of [He] = 0.07 and [He] = 0.15.

In Figure 7 we show these models, together with the one obtained for the standard abundance [He] = 0.1, in the region above $\log m = -3$, where they differ. In Figure 8 we compare

the 10830 and 584 Å profiles obtained with these three models. In general, the differences in the profiles are very small, although a larger value of abundance corresponds to narrower profiles in both lines. This is due to the fact that to compensate for a smaller abundance, the region of formation of the lines needs to be extended to obtain enough helium atoms. This larger region between 1×10^4 and 2.5×10^4 K can be noted in Figure 7 and results in a broader line. Although the ratio between the peaks and the central absorption of the 584 Å changes by a factor of 2 with the extreme abundance values, the convolution with the broad CDS response destroys any difference. Only observations of EUV lines at much higher spectral resolution might then help to discriminate between different abundance values.

5. DISCUSSION AND CONCLUSIONS

We obtained a large set of simultaneous and cospatial observations of an active region, including the chromospheric lines Ca II K, Hα, and Na I D, as well as the He I lines at 5876 (D3), 10830, and 584 Å and the He II line at 304 Å. The EUV radiation in the range $\lambda < 500$ Å and in the range $260 < \lambda < 340$ Å has also been measured at the same time. Using the program PANDORA, we were able to build semiempirical atmospheric models to match this set of observables. The He lines and continua are self-consistently computed in the radiative transfer calculations. In particular, we were interested in the role of the photoionization-recombination process in the formation of the He lines and in the effect of possible variations of [He] in an active region.

One of the main problems for the calculation of the He line profiles was to estimate the total number of ionizing photons impinging on the target active region and their spectral distribution. The adopted procedure combines the observations from CELIAS/SEM and EIT instruments for our region with the synthetic spectrum obtained with the CHIANTI database for an "average" active region and a $P_e/k = 3 \times 10^{15}$ K cm^{-3}. We needed to scale the synthetic spectrum by a factor 1.3 ± 0.3 to obtain the estimated value of I^{corona} (§ 3.2).

To validate this approach we compared the He II 304 Å intensity, measured directly from CDS in the target area, with the one obtained from the SEM$_1$ irradiance in the range $260 < \lambda < 340$ Å, and the agreement was well within the uncertainties. Futhermore, we found that the electron pressure for the most external point of the model for which we have an observational constraint agrees with the one assumed to compute the spectral distribution with the CHIANTI database. The agreement makes us confident that the obtained model is self-consistent with the EUV coronal intensity used.

A semiempirical model with a standard value for [He] and a modified distribution of microturbulence v_t (reduced in the region of formation of the He lines) provides a good agreement with all the observations. However, we must stress that the broad CDS response function heavily conceals the details of the EUV line profiles, thus limiting their diagnostic relevance.

For this model, defined as our standard model, we study the influence of the coronal radiation on the computed helium lines. We find that, similarly to the quiescent case, in an active region the incident coronal radiation has a limited effect on the UV He lines, while it fundamentally affects the D3 and 10830 Å lines. For these latter two lines, the photons of wavelengths between 50 and 100 Å are very effective in increasing the line depth, confirming that for the calculation of the He line profiles it is crucial to correctly estimate the total number of ionizing photons and their spectral distribution. While the assumption of an average distribution might not be critical in the case of a "stationary" active region, this could be not true in the case of a flare, in which the coronal EUV radiation is probably harder.

Finally, we tested how the helium abundance influenced our computed profiles, changing the value of [He] only in the region where the temperatures are larger than 1×10^4 K. We built two more models for [He] = 0.15 and [He] = 0.07 and found that we could match the observations with these models as well as with the standard model. The differences in the computed lines are mostly evident for 584 and 304 Å, whose ratio between the peaks and the central absorption changes by a factor of 2 with the extreme [He] values. However, given the coarse spectral resolution of CDS, they are not appreciable in our observations and hence do not provide enough constraints to choose between [He] values. Observations of the 584 and 304 Å lines with a spectral element smaller than 0.025 Å pixel^{-1} around 584 Å might help in this issue. This resolution for the 584 Å line is currently achieved, in the second order, only by the SUMER spectrograph aboard SOHO. However, SUMER has been restricted to off-limb observations since the year 2000, and the existing archival data do not seem adequate to determine the helium abundance. The SUMER observations do not include the He II Lyα line around 304 Å. Thus, we have to wait for a next-generation EUV spectrograph aboard one of the forthcoming missions such as Solar Orbiter. Furthermore, since the changes of the atmospheric structure with [He] are larger in the transition region, it would be useful to constrain this part of the atmosphere with other observables, independent on the He lines. In particular, we suggest that simultaneous observations of EUV lines of C II, C III, Si II, and Si III might be very important to define the structure of the transition region and hence help to discriminate between [He] values.

APPENDIX

DERIVATION OF INTENSITIES FROM IRRADIANCE MEASUREMENTS

If the Sun were a featureless disk with no limb brightening nor off-limb emission, the disk-integrated flux (irradiance), Φ, measured at a distance D would be easily related to the specific intensity, I, at the solar surface:

$$\Phi = I\pi R_\odot^2/D^2 = I\Omega_\odot,$$

where $R_\odot$ and $\Omega_\odot$ are, respectively, the solar radius and the angular dimension of the solar disk (in steradians).

In the case of a spatially resolved, full-disk solar image where it is possible to identify N discrete structures, each of area S_i ($i = 1 \ldots N$) and emitting a surface intensity I_i along the line of sight, the observed irradiance is

$$\Phi = \sum_i I_i \frac{S_i}{D^2} = \sum_i I_i \Omega_i,$$

where $\Omega_i = S_i/D^2$ is the angular size of the ith structure.

From the above relation, the contribution to the irradiance from the individual structure i is therefore

$$\Phi_i = \left(\frac{I_i \Omega_i}{\sum_j I_j \Omega_j} \right) \Phi.$$

Hence, the surface specific intensity in that structure can be written as

$$I_i = \frac{\Phi_i}{\Omega_i} = c_i \Phi, \tag{A1}$$

where the conversion factor c_i (in units of an inverse solid angle) is

$$c_i = \frac{I_i}{\sum_j I_j \Omega_j}. \tag{A2}$$

The relations (A1) and (A2) are useful if the total irradiance is available in absolute units (e.g., photons cm^{-2} s^{-1}), while a solar image in the same bandpass provides spatially resolved, uncalibrated (e.g., counts pixel^{-1} s^{-1}) intensities. It is also worth noting that the structures in equations (A1) and (A2) can be arbitrary; the intensities I_i can in fact be the intensities of a single pixel or of a set of pixels.

In the limit of continuous intensity distributions, it is easy to generalize those relations to obtain the mean intensity in an arbitrary region $\mathcal{R}$ as

$$\langle I \rangle_\mathcal{R} \equiv \frac{1}{\Omega_\mathcal{R}} \int_\mathcal{R} I \, d\Omega.$$

Hence, the generalization of relations (A1) and (A2) is trivial:

$$\langle I \rangle_\mathcal{R}^{\text{calib}} = \Phi^{\text{calib}} \langle c \rangle_\mathcal{R}, \tag{A3}$$

where the mean conversion factor is

$$\langle c \rangle_\mathcal{R} = \frac{1}{\Omega_\mathcal{R}} \frac{\int_\mathcal{R} d\Omega \, I^{\text{counts}}}{\int d\Omega \, I^{\text{counts}}}. \tag{A4}$$

REFERENCES

Andretta, V., Del Zanna, G., & Jordan, S. D. 2003, A&A, 400, 737
Andretta, V., & Jones, H. P. 1997, ApJ, 489, 375
Andretta, V., Jordan, S. D., Brosius, J. W., Davila, J. M., Thomas, R. J., Behring, W. E., & Thompson, W. T. 2000, ApJ, 535, 438
Athay, R. G. 1988, ApJ, 329, 482
Avrett, E. H., & Loeser, R. 1984, in Methods in Radiative Transfer, ed. W. Kalkofen (Cambridge: Cambridge Univ. Press), 341
———. 2003, in IAU Symp. 210, Modeling of Stellar Atmospheres, ed. N. Piskunov, W. W. Weiss, & D. F. Gray (Dordrecht: Kluwer), A21
Barraclough, B. L., Gosling, J. T., McComas, D. J., & Goldstein, B. E. 1995, in AIP Conf. Proc. 382, Proc. Eighth International Solar Wind Conference (New York: AIP), 73
Bochsler, P. 1998, Space Sci. Rev., 85, 291
Boothroyd, A. I., & Sackmann, I.-J. 2003, ApJ, 583, 1004
Delaboudinière, J.-P., et al. 1995, Sol. Phys., 162, 291
Falchi, A., & Mauas, P. J. D. 1998, A&A, 336, 281
Feldman, U. 1998, Space Sci. Rev., 85, 227
Fontenla, J. M., Avrett, E. H., & Loeser, R. 1991, ApJ, 377, 712
———. 1993, ApJ, 406, 319
Fontenla, J. M., et al. 2002, ApJ, 572, 636
Fredvick, T., & Maltby, P. 1999, Sol. Phys., 184, 113
Gabriel, A. H., Culhane, J. L., Patchett, B. E., Breeveld, E. R., Lang, J., Parkinson, J. H., Payne, J., & Norman, K. 1995, Adv. Space Res., 15(7), 63
Geiss, J. 1982, Space Sci. Rev., 33, 201
Hansteen, V. H., Leer, E., & Holzer, T. E. 1997, ApJ, 482, 498
Hovestadt, D., et al. 1995, Sol. Phys., 162, 441

Judge, D. L., et al. 1998, Sol. Phys., 177, 161
Laming, J. M., & Feldman, U. 2001, ApJ, 546, 552
———. 2003, ApJ, 591, 1257
Lie-Svendsen, Ø., Hansteen, V. H., & Leer, E. 2003, ApJ, 596, 621
Mango, S. A., Bohlin, J. D., Glackin, D. L., & Linsky, J. L. 1978, ApJ, 220, 683
Mauas, P. J., Avrett, E. H., & Loeser, R. 1988, ApJ, 330, 1008
Mauas, P. J. D., Falchi, A., Pasquini, L., & Pallavicini, R. 1997, A&A, 326, 249
McMullin, D. R., et al. 2002, in The Radiometric Calibration of SOHO, ed. A. Pauluhn, M. C. E. Huber, & R. von Steiger (ISSI Scientific Report SR-002; Noordwijk: ESA), 135
Meyer, J.-P. 1996, in ASP Conf. Ser. 99, Cosmic Abundances: Proceedings of the 6th Annual October Astrophysics Conference, ed. S. S. Holt & G. Sonneborn (San Francisco: ASP), 127
Proffitt, C. R., & Michaud, G. 1991, ApJ, 380, 238
Raymond, J. C., et al. 1997, Sol. Phys., 175, 645
Teriaca, L., Falchi, A., Cauzzi, G., Falciani, R., Smaldone, L. A., & Andretta, V. 2003, ApJ, 588, 596
Thomas, R. J., & Neupert, W. M. 1994, ApJS, 91, 461
Thompson, W. T., McMullin, D. R., & Newmark, J. S. 2002, in The Radiometric Calibration of SOHO, ed. A. Pauluhn, M. C. E. Huber, & R. von Steiger (ISSI Scientific Report SR-002; Noordwijk: ESA), 211
Vernazza, J. E., & Reeves, E. M. 1978, ApJS, 37, 485
Young, P. R., Del Zanna, G., Landi, E., Dere, K. P., Mason, H. E., & Landini, M. 2003, ApJS, 144, 135
Zirin, H. 1975, ApJ, 199, L63